nature communications

Article

https://doi.org/10.1038/s41467-025-59020-w

Li^+-migration influencing factors and non-destructive life extension of quasi-solid-state polymer electrolytes

Received: 8 October 2024

Accepted: 9 April 2025

Published online: 19 April 2025

Check for updates

Peiying Li[1,5], Jinjin Hao[1,5], Shuang He[1,5], Zenghua Chang[2,5], Xiaolei Li[1], Rennian Wang[2], Wen Ma[3], Jiantao Wang[2], Yuhao Lu[3], Hong Li[4], Liqun Zhang[1] & Weidong Zhou[1]

Polymer-based quasi-solid-state electrolytes (QSSE) are believed to be the most feasible candidates for solid-state batteries, but they are hindered by relatively lower ionic conductivity and narrower electrochemical window. Here, we synthesize a series of ether-free acrylates containing Li^+-ligands for high-voltage-stable QSSEs. Our findings demonstrate that the polymer-involved solvation structure is critical in determining the ionic conductivity, and low-temperature crystallization of the polymer can be used for non-destructive life extension of batteries. The prepared polymers do not contain ether unit and exhibit a polymerization degree of 99% in cells without residual double-bonded monomer, endowing them with high antioxidation capability and compatibility with high-voltage positive electrodes including $LiNi_{0.85}Co_{0.075}Mn_{0.075}O_2$, 4.6 V $LiCoO_2$ and 4.8 V $Li_{1.13}Ni_{0.3}Mn_{0.57}O_2$. The confinement of liquid in QSSEs effectively suppresses the interfacial reactions, but the residual interface reactions still gradually consume liquid electrolytes and cause capacity fading, due to the limited diffusion of the confined solvent to wet the interface. Through crystallizing the polymer matrices at −50 °C, the confined liquid in QSSEs is released and re-wets the Li-metal/polymer interface, thereby recovering the capacity and extending the life of solid-state batteries in a non-destructive manner.

With the rapidly growing application of lithium-ion batteries in various fields, especially in electric vehicles, the demands for energy density and safety have become increasingly urgent[1,2]. To satisfy these requirements, the employment of solid-state electrolytes to replace traditional liquid electrolytes is an effective strategy, since the solid electrolytes have better compatibility with large-capacity Li-alloy negative electrode and are less flammable[3–6]. Among all kinds of solid-state electrolytes, solid polymer electrolytes (SPEs) show advantages in better flexibility, closer interfacial contact, lower cost, and higher stability in air[7,8]. Despite these advantages of SPEs, the relatively lower ionic conductivity and narrower electrochemical windows are two barriers for their application[9–11]. To improve the ionic conductivity, the liquid-containing quasi-solid-state electrolytes (QSSE) were proposed, which significantly enhance the Li^+-conductivity[12–14]. In this field, the in situ polymerized QSSEs are preferred, owing to better compatibility with the current commercial assembly line of cells[15].

Currently, the double bond radical polymerization (DBRP) is the most widely studied in situ polymerization in cells, in which,

[1]Beijing Advanced Innovation Center for Soft Matter Science and Engineering, State Key Laboratory of Organic-Inorganic Composites, Beijing University of Chemical Technology, Beijing, China. [2]China Automotive Battery Research Institute Co. Ltd. Beijing, Beijing, China. [3]Ningde Amperex Technology Limited (ATL), Key Laboratory of Consumer Lithium-Ion Battery in Fujian, Fujian, China. [4]Key Laboratory for Renewable Energy, Institute of Physics, Chinese Academy of Sciences, Beijing, China. [5]These authors contributed equally: Peiying Li, Jinjin Hao, Shuang He, Zenghua Chang. e-mail: zhouwd@mail.buct.edu.cn

poly(ethylene glycol) methyl ether methacrylate (PEGMA), vinylethylene carbonate (VEC), and vinylene carbonate (VC) are three types of mostly used monomers[16–18]. Nevertheless, PEGMA contains a ether chain, making it easily be oxidized by high-voltage positive electrodes (Fig. 1a). VEC and VC show a lower polymerization degree of 50-80%, and the residual double bonds tend to be oxidized at higher than 4.3 V[19]. Although there are many reports of polymer electrolytes suitable for high voltage positive electrodes, these cells are rarely charged to higher than 4.5 V (Supplementary Table 1). In addition, compared with the Li^+-hopping in liquid-free polymer electrolytes, the Li^+-migration mode in QSSEs is still unclear, which is necessary for the design of future QSSEs (Fig. 1b). What's more, although the interfacial reactions are largely suppressed, the residual interfacial reactions of liquid in QSSEs with Li-metal still cause liquid depletion on interface and the subsequent resistance increase, since the liquid could not diffuse freely (Fig. 1c). To obtain a high performance polymer-based QSSE, the following requirements should be satisfied (Fig. 1d): (1) a high polymerization degree in cells without residual monomers, as monomers may contain easily oxidized polymerization sites; (2) high polymer-solvent affinity for lower polymer-solvent barrier and strong confinement of liquid electrolytes, which is better when liquid could also be released controllably, (3) suitable solvation capability of polymer and solvent with Li^+ for easier Li^+-migration. In addition, compared to other kinds of solid electrolytes, the cost advantages of SPE, including both polymer and Li-salt, should also be maintained (Fig. 1e and Supplementary Fig. 1), which is a critical factor for the large-scale application.

Considering the high DBRP efficiency of acrylates in the presence of Li-metal, the ether-free acrylate-based monomers are desired candidates for the construction of high-voltage stable SPEs. Here, a family of ether-free acrylate-based monomers containing Li^+-ligands were developed for in situ solidified high-voltage stable electrolytes, including (2-oxo-1,3-dioxolane-4-yl)methyl acrylate (DOA), 2-((propoxycarbonyl)oxy)ethyl acrylate (PCEA), 2-(acryloyloxy)ethyl ethyl oxalate (AEEO), 2-acrylamidoethyl propyl carbonate (AAPC) and 2-acrylamidoethyl ethyl oxalate (AAEO). In the presence of Li-metal and oxide positive electrodes, all five monomers show high polymerizing conversions of nearly 100%, without obvious monomer left, avoiding the otherwise oxidation of double bonds in monomers. With the presence of 30 wt% monomers in liquid electrolytes, QSSE membranes can be obtained after polymerization, giving a conductivity of over 1.0×10^{-3} S cm^{-1}. It is observed that the ionic conductivity is significantly affected by the polymer-solvent affinity and solvation structure. A strong polymer-solvent affinity is beneficial to the generation of homogenous gel and the continuous Li^+-transport, while a poor polymer-solvent affinity would generate micro phase-separation and inhibit the Li^+-transport. For the Li^+ solvation structure, the mobile solvent with a stronger solvation capability is helpful for Li^+-migration since it moves with Li^+. By contrast, for the immobile polymer chains, a weaker solvation capability makes de-solvation and Li^+-hopping easier. Using the in situ polymerization of these monomers, the QSS Li||NCM85 ($LiNi_{0.85}Co_{0.075}Mn_{0.075}O_2$), Li||LCO ($LiCoO_2$) and Li||LRMO ($Li_{1.13}Ni_{0.3}Mn_{0.57}O_2$) cells were fabricated, showing the capacity retention of 80 ± 5% after 500 cycles for Li||NCM85 at 1 C (0.40 mA cm^{-2}) and 300 cycles for Li||LCO at 1 C (0.44 mA cm^{-2}), and 91% after 100 cycles for Li||LRMO at 0.2 C (0.044 mA cm^{-2}) at 25 ± 1 °C, verifying the high voltage stability of these QSSEs. Although the QSSEs suppress the interfacial reactions to a large extent, the residual interface side reactions with Li-metal still gradually consume liquid electrolytes at the interface and cause capacity fading. By means of the crystallization of polymer at a lower temperature (−50 °C), polymer-solvent phase separation occurs and the originally confined liquid in QSSE is released, which re-wet the interface of Li/polymer. When rewarming to room temperature, the polymers reabsorb liquid and regenerate amorphous QSSE, reconstructing the Li/polymer interface with recovered capacity, giving a way for the non-destructive life extension of QSS batteries.

Results

Polymerization of monomers in various liquid electrolytes for QSSEs

To dissociate Li-salt, Li^+-coordinating units of ethylene carbonate (EC) or diethyl carbonate (DEC), or diethyl oxalate (DOE) were connected to acrylate through an ester or amide bridge (Fig. 2a, Supplementary Figs. 2–6 and Supplementary Table 2), without employing any ether unit for improving the antioxidation capability[20–22]. To investigate the compatibility of these polymers with various liquid electrolytes, seven electrolyte formulas of dimethyl carbonate (DMC), DEC, EC, propylene carbonate (PC), EC-DMC (1:1), EC-DEC (1:1), and EC-DEC-FEC (Fluoroethylene carbonate) (2:1:1) with 1.1 M $LiPF_6$ were tested. The weight

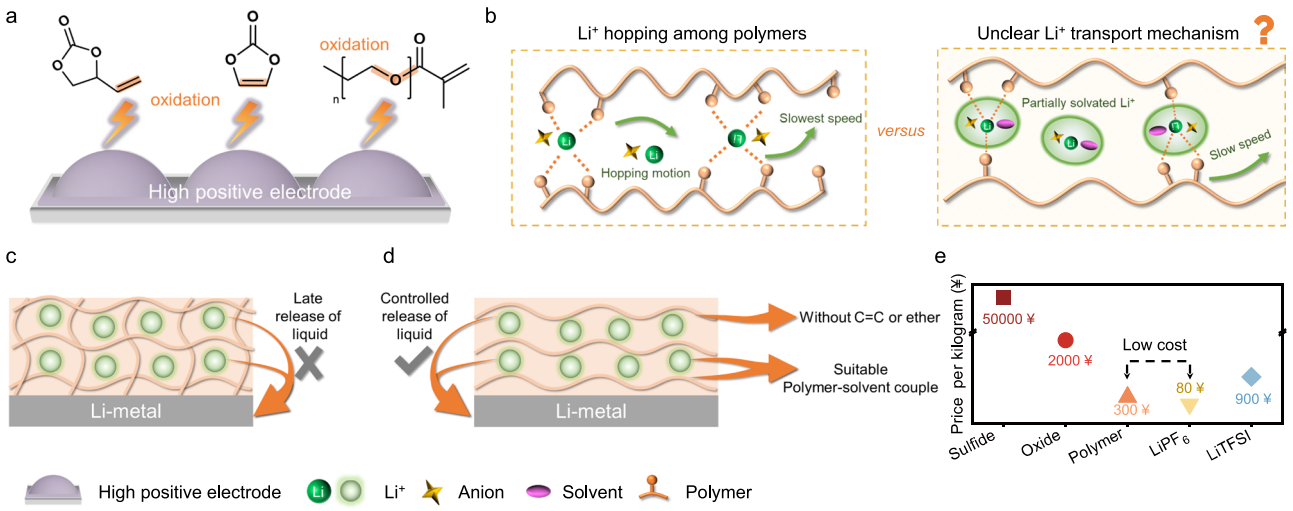

Fig. 1 | Challenges and requirements of QSSEs in solid-state batteries. **a** Oxidation of VEC, VC and PEGMA in high-voltage positive electrode cells. **b** Unclear Li-migration mechanism in polymer-based quasi-solid-state electrolytes (QSSE). **c** Late release of liquid on the interface with Li-metal and increased resistance. **d** The requirements of desired QSSEs in high-voltage cells. **e** The cost comparison of various solid electrolytes, including sulfide electrolytes, oxide electrolytes, polymer, and Li-salt. All price was calculated from industrial products in Chinese Yuan (¥).

https://doi.org/10.1038/s41467-025-59020-w

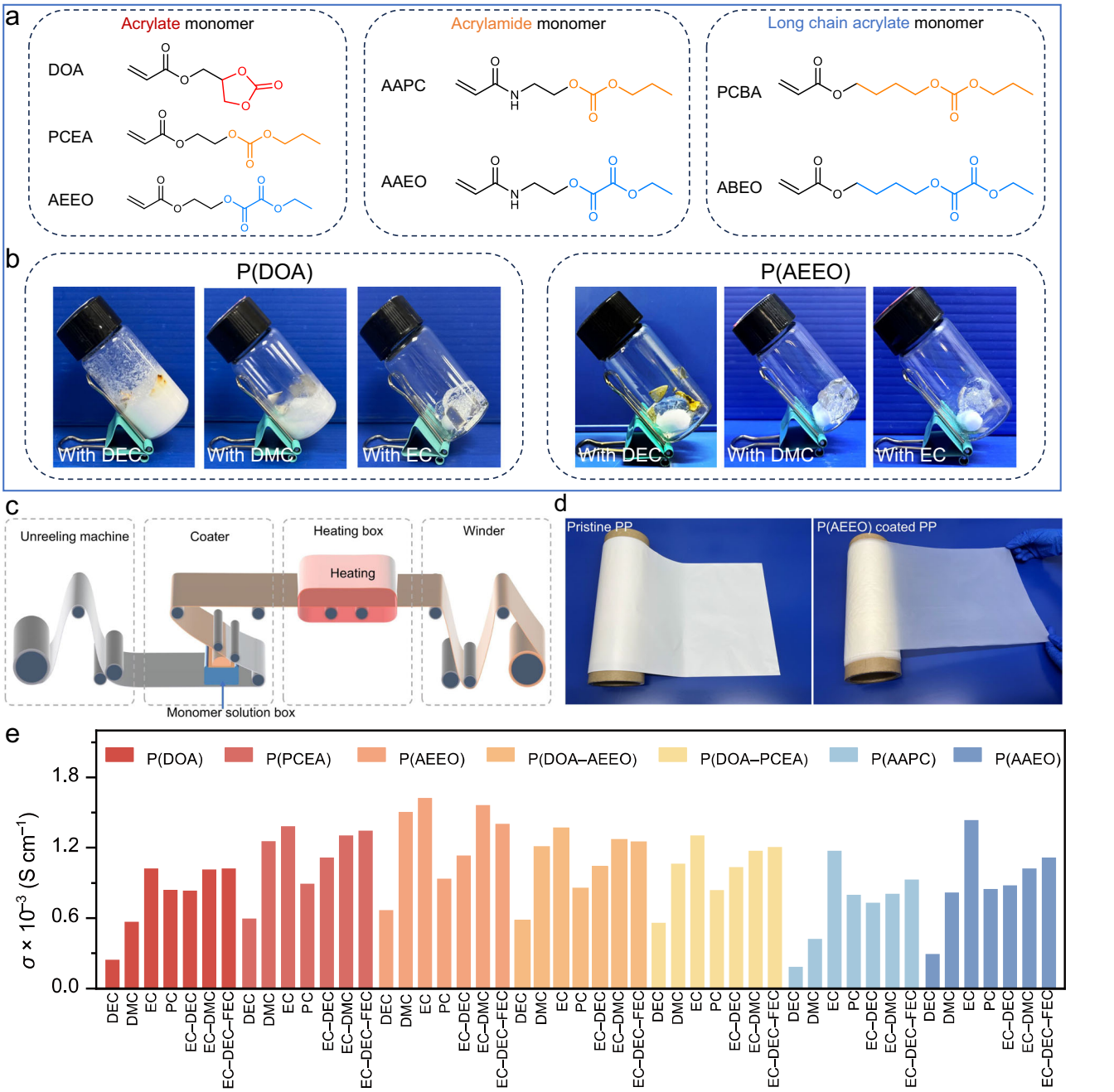

Fig. 2 | Structures of monomers, polymerization of polyesters, and corresponding ionic conductivity. a Ester bridged DOA, PCEA, and AEEO, and amide bridged AAPC and AAEO monomers and two longer chain derivatives. **b** Images of polymerized DOA and AEEO monomers in different liquid electrolytes of EC, DMC, or DEC. **c** Continuous in situ polymerization line on porous polypropylene (PP) separators. **d** The image of bare and P(AEEO) coated PP separators. **e** The summarized ionic conductivity of seven QSSEs with various solvents of EC, PC, DMC, DEC, EC-DEC (1:1), EC-DMC (1:1) or EC-DEC-FEC (2:1:1) (containing 30 wt% polymer, 16 wt% $LiPF_6$ and 54 wt% liquid solvents).

ratio of polymer was controlled constantly at 30 wt%, and the concentration of $LiPF_6$ was maintained at 1.1 M (~16 wt%), with the liquid solvents accounting for ~54 wt%. Li-foil was added to the mixture of solvent, monomer, and azobisisobutyronitrile (AIBN) catalyst, which was then heated to 55 °C to initiate the thermal polymerization. All these liquid solutions turned into solid-state gels after 1 hour and were maintained at 45 °C for another 12 hours to ensure the completion of polymerization (Fig. 2b and Supplementary Figs. 7 and 8), indicating Li-metal did not prevent the polymerization, which is desired for the in situ solidification of electrolyte in the Li-metal containing cells. The acrylate group shows a near 100% polymerization rate (Supplementary Figs. 9 and 10), significantly higher than that of the widely studied VEC and VC (50-80%), avoiding the otherwise oxidation of residual double bond-containing monomers at high voltage[23].

Among all these electrolyte formulas, it is observed P(DOA) generates white opaque gels in DEC or DMC electrolyte (Fig. 2b), which can be attributed to the phase separation between P(DOA) and DEC or DMC. In all the other solvents, P(DOA) forms transparent and colorless gels without any flowable species. The other four polymers of P(PCEA), P(AEEO), P(AAPC), and P(AAEO) generate transparent solid-gels in all seven kinds of solvents, indicating better affinity towards these liquid solvents. Both copolymers of P(DOA-PCEA) and P(DOA-AEEO) form opaque gels in DEC electrolyte but transparent solid-gel in all the other liquid electrolytes

(Supplementary Fig. 8). In addition, it is observed that Li-foil turns yellow or black in all these DEC-contained composites; while in all the other solvent formulas, the Li-foils still remain flashing after polymerization, which can be attributed to a heavier interfacial reaction of DEC with Li-foil (Supplementary Fig. 11)[24,25]. Under the same liquid solvents, DOA shows the quickest polymerization speed, and the generated solid-gels own the strongest stiffness, followed by amide-containing P(AAPC) and P(AAEO) gels, then P(AEEO) and P(PCEA). 30 wt% P(DOA) based QSSEs generate self-standing membranes with a thickness of 20–30 μm (Supplementary Fig. 12). This difference in polymerization speed and stiffness can be attributed to the interchains' aggregation. Stronger interactions among planar cyclic carbonate units in P(DOA) and hydrogen bonds in amide-containing P(AAEO) and P(AAPC) shorten the intermolecular distance, accelerate the polymerization speed, and enhance the stiffness of corresponding gels. To detect the liquid confinement capability of polymers, the state of QSSEs was monitored with the gradual increase of liquid (EC-DEC-DEC, 2:1:1) in the presence of 1.1 M $LiPF_6$ (Supplementary Fig. 13). The P(DOA), P(PCEA), and P(AEEO) composed gels start to show flowability when the polymer content is reduced to 15 wt%. Whereas P(AAPC) and P(AAEO) composed gels still maintain solid-state until the polymer content is reduced to 5 wt%, indicating that the hydrogen bonds in amide units enhance the liquid confinement capability.

Through the in situ polymerization in/on porous polypropylene (PP) separators, the original pores in the separator were filled by polymers (Fig. 2c, d and Supplementary Figs. 14 and 15). Comparing the ^{1}H NMR spectra of monomer and in situ polymerized polymers in PP separator, the monomer conversion rate reaches 99%, without obvious double bond signals left, same to the polymerization degree in vials (Supplementary Figs. 16–19). But the in situ polymerization in/on the separator gives a molecular weight of ~300 K, smaller than that obtained in vials (over 600 K), owing to the confining effect of nanopores in the separator (Supplementary Fig. 20 and Supplementary Table 3). Even if a slightly lower *M*w was reached, the obtained membranes still show dry and non-sticky surface and can be prepared into rolls in the continuous production line, which can be used in the assembly of large single cell of over 300 Ah, since the in situ polymerization of monomers within this kind of large cell is hard to be uniform (Fig. 2d).

For all kinds of polymers, EC-containing QSSEs deliver the highest Li^+-conductivity, reaching 1.02×10^{-3}, 1.38×10^{-3}, 1.62×10^{-3}, 1.37×10^{-3}, 1.30×10^{-3}, 1.17×10^{-3} and 1.43×10^{-3} S cm^{-1} at room temperature for P(DOA), P(PCEA), P(AEEO), P(DOA-AEEO), P(DOA-PCEA), P(AAPC) and P(AAEO), respectively (Fig. 2e). This higher Li^+-conductivity of EC-containing QSSEs can be attributed to a stronger polarity of EC and higher dissociation of Li-salt[20,26,27]. The ionic conductivities of all these QSSEs with DMC are around 2.0–2.5 times of that with DEC, owing to a smaller size of DMC and less steric hindrance in polymer chains. In the mixed solvents of EC-DMC (1:1), EC-DEC (1:1), and EC-DEC-FEC (2:1:1), intermediate conductivities were obtained, higher than those of QSSEs with single DMC and DEC solvents, but lower than those of QSSEs with only EC, further verifying the significant contribution of EC. Under the same solvent systems, P(AEEO) delivers the highest Li^+-conductivity and then P(AAEO) and P(PCEA), followed by P(DOA-AEEO) and P(DOA-PCEA), and then P(AAPC), while P(DOA) shows the lowest conductivity (Supplementary Fig. 21). This also can be attributed to the stronger coordination of EC unit from P(DOA) with Li^+, which suppresses the migration of Li^+, since the polymer could not migrate with Li^+. In addition, it is observed that when increasing the carbon chain of the ester bridge from two carbon to four carbon, the Li^+-conductivity does not show obvious increase (Supplementary Fig. 22), indicating the carbon linker does not influence the ionic conductivity significantly, and the ionic conductivity is more affected by the solvents and coordinating units in polymers.

Solvation structures of QSSEs

Considering the conductivity of these QSSEs varies significantly with the change of solvents and polymers, the interactions of polymers and solvents with Li-salt should play critical roles[28,29]. As shown in the ^{1}H NMR titration results (Fig. 3a–c), in the absence of Li-salt, with the increase of P(DOA) in three solvents of DEC, DMC, and EC, the ^{1}H NMR signals of these solvents underwent obvious high-field shift, indicating the increased shielding effect from polymer. It is observed that the shifted values of ^{1}H NMR signals are in the order of EC > DMC > DEC, indicating a stronger affinity between P(DOA) and EC. DEC underwent the smallest shift with the increment of P(DOA), implying the weakest interaction between DEC and P(DOA), possibly owing to a larger steric hindrance of DEC, making DEC more difficult to enter the P(DOA) matrix. The same trend and effect were also observed when monitoring the change of FT-IR (Fourier transform infrared) spectra, where the C=O vibration of P(DOA) shifted to higher wavenumbers with the increase of solvent (Supplementary Fig. 23), and the redshift values were also in the sequence of EC > DMC > DEC, demonstrating the higher affinity of EC and P(DOA). When moved to other polymers, the ^{1}H NMR chemical shift of solvent molecules also moved toward high-field and the moved values of EC and DMC are obviously larger than that of DEC, implying the shielding effect from polymer on EC and DMC is heavier than that on DEC (Fig. 3g–i and Supplementary Fig. 24). In addition, the FT-IR spectra of these polymers show larger shift when combined with EC and DMC than with DEC, verifying weaker interaction with DEC.

With the presence of $LiPF_6$, the ^{1}H NMR chemical shifts of solvents moved toward high-field relative to the counterparts without Li-salt, and the FT-IR spectra of polymer also moved toward high wavenumbers compared with the counterparts without Li-salt, indicating polymer involved the coordination with Li^+ (Fig. 3d–f, j–l and Supplementary Figs. 24 and 25). These features can be attributed to the electronic transfer from C=O to Li^+ and the following increased polarization degree, which enhanced the C-H strength (Supplementary Fig. 26)[25,30]. The moved degree is obviously higher in EC than in DMC and then DEC, verifying the relatively stronger interaction of EC with Li^+, in agreement with the Li^+-conductivity[20,26]. As for the larger shift in DMC than in DEC, possibly owing to a bigger steric hindrance of DEC, making DEC more difficult to enter polymer matrix. TGA test of QSSEs also demonstrates the interactions between solvents and polymers. It is observed that the initial weight loss temperatures of solvents in QSSEs are higher than those of corresponding solvents in liquid electrolytes, which verifies the solvent-polymer interactions (Fig. 3m and Supplementary Figs. 27 and 28). Additionally, the increased degree of the initial weight loss temperature of EC in QSSEs is greater than that of DEC in QSSEs, indicating that EC has stronger interactions with these polymers, which is consistent with the results from NMR and FT-IR analyses. This relatively weaker interaction of DEC with these polymers and Li^+ is exemplified by P(DOA) and DEC, which leads to the micro phase separation between liquid DEC and solid P(DOA). In this case, Li-salt is mainly dissolved in the liquid capsules instead of dry polymer, which generates a liquid/polymer barrier and prevents the continuous Li^+ transport (Fig. 3n)[31]. On the contrary, a stronger affinity between polymer and solvent would generate homogeneous QSSEs and facilitate the Li^+-migration.

Among different coordinating units with Li^+ here, EC possesses obviously higher dielectric constant than DEC and oxalate (Supplementary Fig. 29). Under the constant molar ratio of solvent: monomer-fragment: Li at 6:2:1 (similar to the molar ratio in these QSSEs) (Supplementary Fig. 30, 31), EC solvent containing P(DOA) and P(AEEO) QSSEs show 3.1-3.2 EC in the primary shell of Li^+ solvation structure (Fig. 4a–d), along with 1.2 or 0.8 carbonyl units from P(DOA) or P(AEEO), respectively, without any undissociated PF_6^- in the primary shell. Whereas the Li^+ solvation structures of DEC-contained P(DOA) and P(AEEO) QSSEs have around 2.6-3.0 DEC in the primary shell,

https://doi.org/10.1038/s41467-025-59020-w

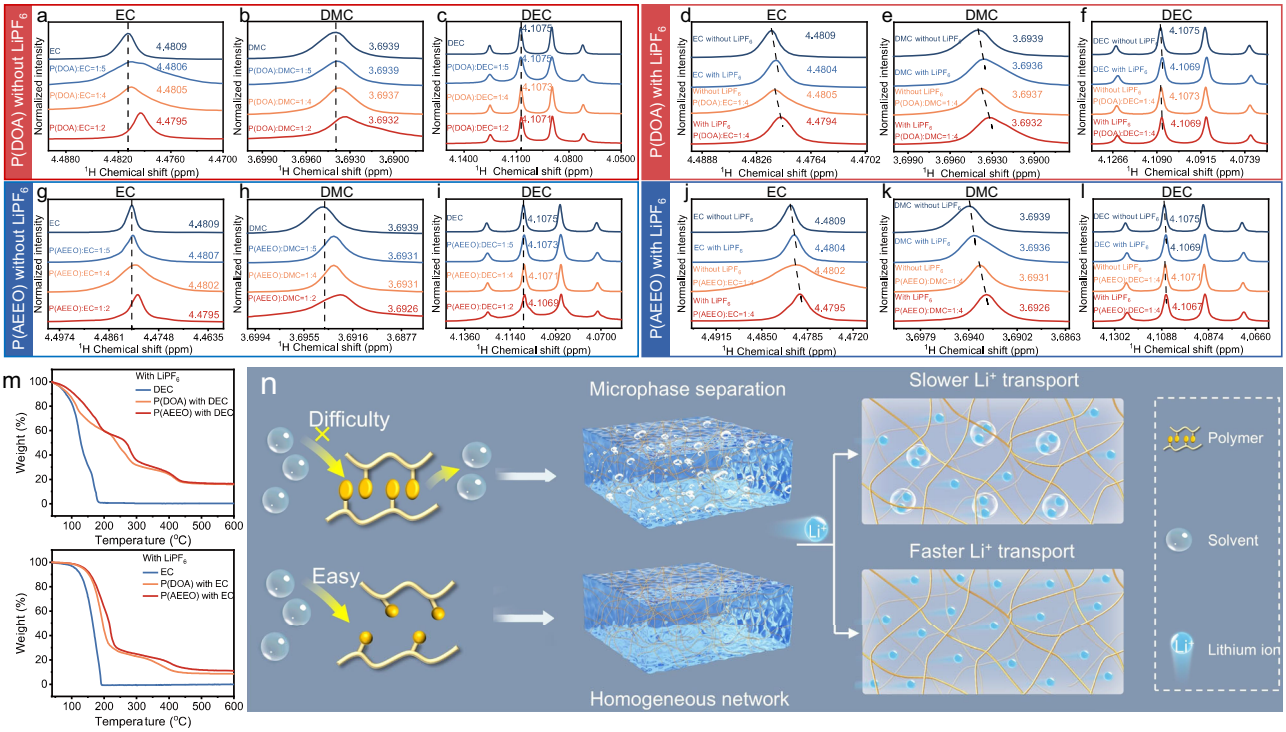

Fig. 3 | Interactions of solvent, polyesters, and Li$^+$. a–c ^{1}H NMR spectra of P(DOA) in different solvents of EC, DMC, or DEC with various molar ratios. **d–f** ^{1}H NMR spectra of P(DOA) in the presence of Li$^+$ and different solvents of EC, DMC, or DEC. **g–i** ^{1}H NMR spectra of P(AEEO) in different solvents of EC, DMC, or DEC with various molar ratios. **j–l** ^{1}H NMR spectra of P(AEEO) in the presence of Li$^+$ and different solvents of EC, DMC, or DEC. **m** The thermal gravimetric analysis (TGA) curves of P(DOA) and P(AEEO) in the presence of 1.1 M $LiPF_6$ and DEC or EC. **n** Proposed Li$^+$ transport models in homogeneous gel and microphase-separated gel.

together with 1.6 or 0.9 carbonyl units from P(DOA) or P(AEEO), respectively, and additional 0.4–0.6 undissociated PF_6^-, indicating a relatively weaker coordination capability of DEC. Experimentally, the ^{7}Li NMR peak of EC-containing P(DOA) and P(AEEO) QSSEs appears at a higher field than DEC-containing counterparts, verifying a relatively weaker coordination capability of DEC than EC (Supplementary Fig. 32). These features result in a significantly higher Li$^+$-conductivity of EC-based QSSEs than DEC-containing counterparts. In the mixed EC-DEC (1:1), P(AEEO) composed QSSE have ~3.2 solvent molecules in the primary Li$^+$-solvation shell, slightly more than that in P(DOA) composed QSSE (~3.0), since oxalates in P(AEEO) own weaker coordination capability than EC and DEC solvents (which is demonstrated by a lower field ^{7}Li NMR peak in DOE with 1.1 M $LiPF_6$, as shown in Fig. 4e and Supplementary Fig. 33), resulting more liquid solvent in primary Li$^+$-solvation shell of P(AEEO) composed QSSE. The EC units in P(DOA) possess similar coordination capability with liquid EC solvent, stronger than DEC, causing less liquid solvent in the primary Li$^+$-solvation shell of P(DOA) based QSSE, which is demonstrated by a higher field ^{7}Li NMR peak in P(DOA) based QSSE than P(AEEO) based QSSE with the same solvents, implying the coordination capability of P(AEEO) with Li$^+$ is lower than P(DOA) (Supplementary Fig. 32). These features endow a higher Li$^+$-conductivity of P(AEEO) composed QSSEs than P(DOA)-based counterparts, which is also verified by the relatively lower de-solvation energy of P(AEEO) composed QSSEs with all these solvents (Fig. 4f and Supplementary Figs. 31–35 and Supplementary Data 1–18). In QSSEs, an intermediate Li$^+$-migration mode between liquid solvent and dry polymer should be exited (Fig. 4g). The vibration of polymer chains facilitates the dissociation of polymer-Li$^+$ complex and allows the Li$^+$ hopping from one fragment to another, but the coordinating units of polymer can't move with the migration of Li$^+$[26,32]. The partially solvated Li$^+$ ions move during charge-discharge, and a relatively weak coordination with Li$^+$ from polymer chains is beneficial to the Li$^+$-migration; while a stronger coordination of liquid solvent with Li$^+$ is helpful for the Li$^+$-migration. This Li$^+$ transport mode is also verified by the liquid content titration experiment results (Supplementary Fig. 36), where the low content liquid from 5 wt% to 15 wt% only improves the ionic conductivity from 9.77×10^{-7} to 4.54×10^{-6} S cm^{-1}, but the ionic conductivity starts to show a sharp increase when the liquid content increasing to over 25 wt%. Under 15 wt% liquid content, the solvent molecules in the Li$^+$ solvation shell are less than 2, and Li$^+$ cations are mainly coordinated by polymer, which is not enough to stimulate Li$^+$ migration. When liquid content is larger than 25 wt%, there are roughly three liquid molecules in the solvation shell of Li$^+$, and allow the formation of partially solvated Li$^+$, facilitating the Li$^+$-migration.

It is obvious that two effects influence the Li$^+$-migration of QSSEs, polymer-solvent affinity and the coordinating capability of solvent/polymer with Li$^+$. Closer polymer-solvent affinity facilitates the generation of homogeneous polymer-solvent composite without micro phase-separation, benefiting the continuous Li$^+$-migration in QSSEs (Fig. 3n). By contrast, weaker polymer-solvent affinity results in the micro phase-separation of polymer and solvent, hindering the Li$^+$-migration. In addition, the coordinating interaction and solvation structure of Li$^+$ with polymer/solvent are also critical for the Li$^+$-conductivity. For mobile liquid molecules, stronger polarity and coordinating capability are helpful for Li-salt dissociation and so Li$^+$-migration (Fig. 4g). But for immobile solid polymer chains, since they can not move with the migration of Li$^+$, a relatively weak interaction with Li$^+$ is beneficial to the de-solvation and so the improvement of ionic conductivity[32]. EC solvent owns stronger solvation capability and better affinity with polymers than DMC and DEC, resulting in higher ionic conductivity of EC-based QSSE. DEC-contained QSSEs show the lowest conductivity, owing to the lowest solvation capability and poorest polymer-solvent affinity. However, for the polymers, the carbonyl oxygen (C=O) in cyclic carbonate of P(DOA) owns stronger coordination with Li$^+$ than linear carbonate of P(PCEA) and then

https://doi.org/10.1038/s41467-025-59020-w

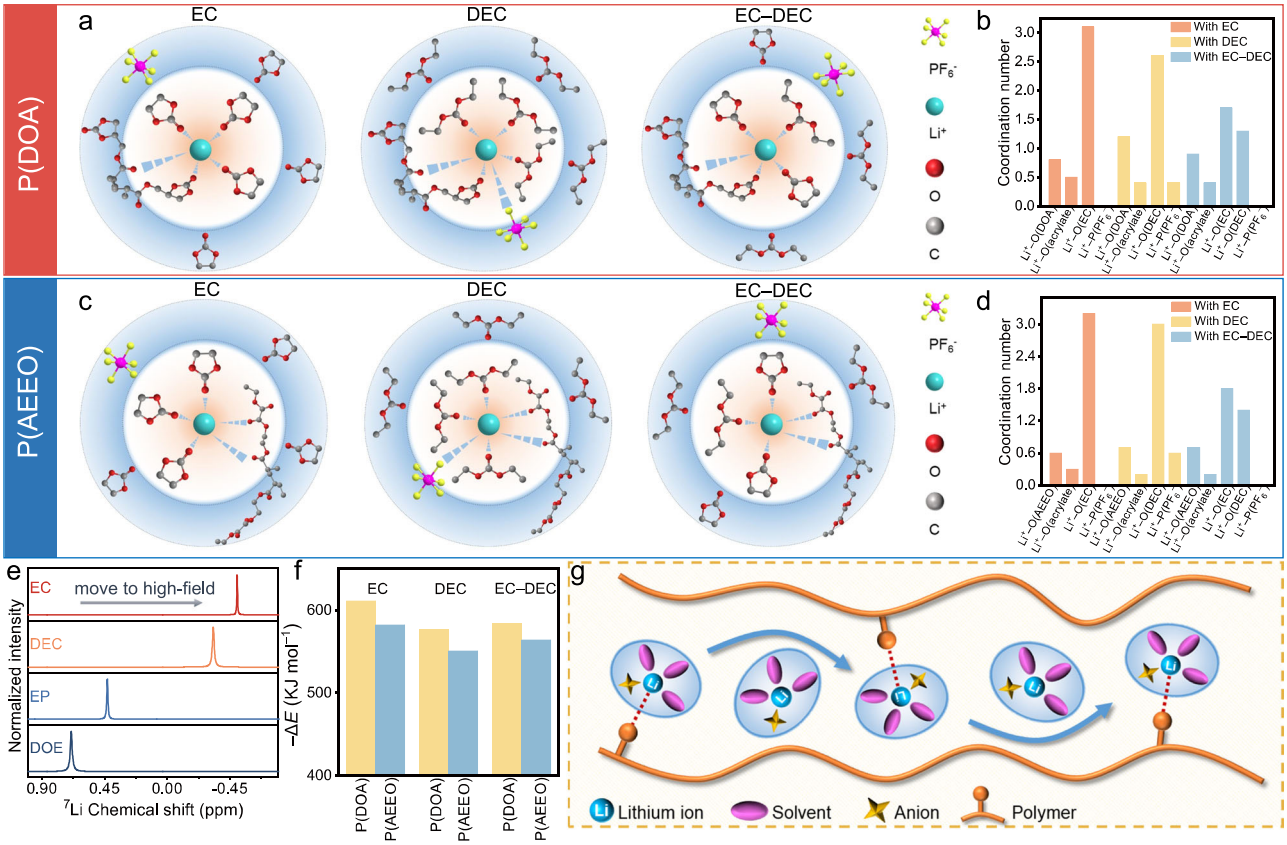

Fig. 4 | Solvation structures of QSSEs. a, **b** The molecular dynamics (MD) simulated solvation structure and coordination number of P(DOA) based QSSEs with 1.1 M $LiPF_6$ and the liquid solvents of EC, DEC, or EC-DEC (1:1). **c**, **d** The solvation structure and coordination number of P(AEEO) based QSSEs with 1.1 M $LiPF_6$ and the liquid solvents of EC, DEC, or EC-DEC (1:1). **e** The ^7Li NMR spectra of 1.1 M $LiPF_6$ in different solvents of EC, DEC, EP (Ethyl propionate), and DOE. **f** The density functional theory (DFT) calculated de-solvation energy (−Δ*E*) of P(AEEO) and P(DOA) based QSSEs in **a** and **c**. **g** The proposed Li^+-migration mode in polymer and solvent composed QSSEs.

oxalate of P(AEEO), leading to the lowest ionic conductivity of P(DOA) but highest conductivity of P(AEEO) based QSSE. On the other extreme condition, when polymers possessing no interaction with Li^+, like a polymeric diluter in liquid electrolytes, the polymer phase would tend to separate from Li^+-coordinated solvent and is not conducive to Li^+-migration.

Reversible polymer crystallization in QSSEs

After holding at −50 °C for 10 hours, the DSC (differential scanning calorimetry) positive scanning of P(DOA), P(AEEO), and P(AAEO) composed QSSEs show obvious endothermic peaks at −22, −36, and −28 °C, respectively, indicating the occurrence of polymer crystallization in QSSEs at low temperature (Fig. 5a–c and Supplementary Fig. 37)[33]. As also verified in the WAXS (wide−angle X−ray scattering) spectra at Fig. 5d–f, no crystal scattering peak is observed at 25 °C. But when the temperature is cooled down to −25 °C and kept at −25 °C for 1 hour, the crystal scattering peaks clearly emerge[34]. With the temperature further lowering to −50 °C for 1 hour, the crystal scattering peaks become much stronger, and then with the temperature rising back to 25 °C, the scattering peaks disappear again (Supplementary Fig. 38), indicating the amorphous QSSEs are recovered. The same trend and effect are also observed when monitoring the change of XRD (X-ray diffraction) patterns, where the intensity of diffraction peaks increases with the decrease of testing temperature and becomes weak again when returning to room temperature (Fig. 5g–i and Supplementary Fig. 39), implying the existence of reversible low-temperature crystallization behavior for QSSEs. At the same time, when these three QSSEs were maintained at −50 °C, the Li^+-conductivity increased gradually with the extension of standing time and then stabilized after 15 hours (Fig. 5j–l), which can be attributed to the low-temperature crystallization of polymers and the following release of the originally confined liquid solvent, with the following generation of connected liquid channels for faster Li^+-migration (Fig. 5m). Considering this polymer crystallization is a physical process and could reversibly release-absorb liquid solvents, this low-temperature crystallization of QSSEs can be utilized to in situ rewet the interface in cells.

Electrochemical properties of QSSEs

The electrochemical window and interfacial stability with Li-metal are critical for the application of QSSEs in solid-state Li-metal cells and the enhancement of energy density. To investigate the antioxidation capability of these polymers, their electrochemical floating tests were carried out in Li||NCM85 cells using the QSSEs with EC-DEC-FEC (2:1:1, 30 wt% polymer and 54 wt% liquid). The leakage currents of P(DOA), P(PCEA), P(AEEO), P(DOA-AEEO), P(DOA-PCEA), P(AAPC), and P(AAEO) based QSSEs are all below 10 μA even when charging to 5.0 V (Fig. 6a, Supplementary Fig. 40), indicating the high stability of these QSSEs at high voltage. On the contrary, the leakage current of P(VEC), P(VC) and P(PEGMA) show sharp increase when higher than 4.5 V, especially for P(PEGMA), indicating their poor stability at high voltage (Fig. 6b). Compared with P(VEC) or P(VC), the higher antioxidation capability of P(DOA), P(PCEA), P(AEEO), P(AAPC), P(AAEO) and their copolymers can be attributed to their high polymerization degree and no residual double bonds containing monomer, since the double bonds could be oxidized at 4.3-4.5 V[35,36]. In addition, the ether group containing P(PEGMA) has been well demonstrated to be easily oxidizable by high-

https://doi.org/10.1038/s41467-025-59020-w

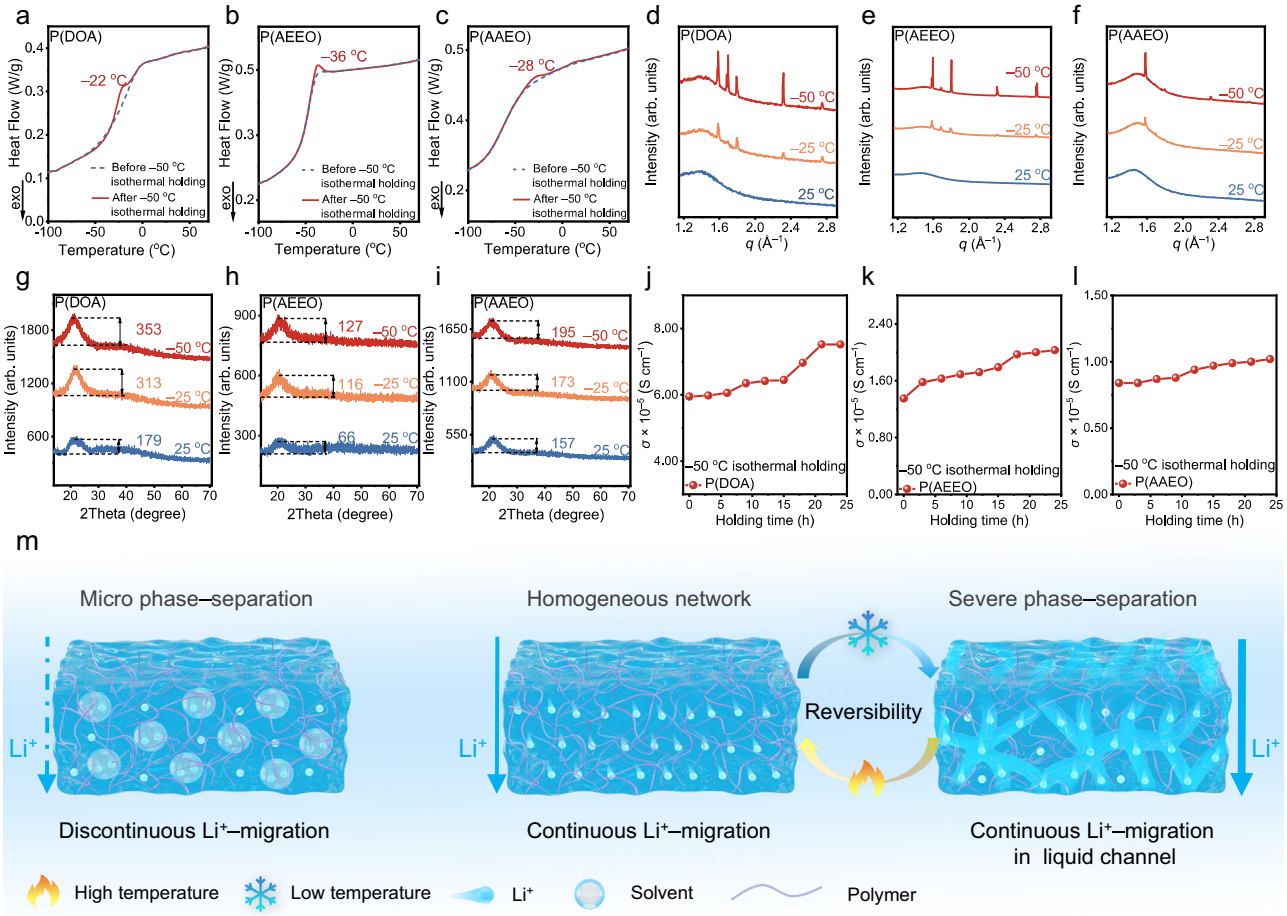

Fig. 5 | Investigation of temperature-responsive crystallization of QSSEs. **a**–**c** DSC (differential scanning calorimetry) curves of P(DOA), P(AEEO), P(AAEO) based QSSEs before and after −50 °C isothermal holding. **d**–**f** WAXS (wide-angle X-ray scattering) curves of P(DOA), P(AEEO), P(AAEO) based QSSEs at different temperatures of −50 °C, −25 °C, or 25 °C. **g**–**i** XRD (X-ray diffraction) patterns of P(DOA), P(AEEO), P(AAEO) based QSSEs at different temperatures of −50 °C, −25 °C or 25 °C. **j**–**l** The Li^+-conductivity of P(DOA), P(AEEO), P(AAEO) based QSSEs holding at −50 °C for different times. **m** Diagram of low-temperature crystallization of QSSEs and corresponding Li^+-migration modes.

voltage positive electrode, which also verifies the necessity of developing ether-free SPEs[37].

In the CV curves of P(DOA), P(PCEA), P(AEEO), P(DOA-AEEO), P(DOA-PCEA), P(AAPC) and P(AAEO) based QSSEs, when $LiPF_6$ is employed, the current intensities of all QSSEs contained Li||Fe (stainless steel, SS) cells undergo a progressive increase in initial 3 cycles and then become stable after the 4th cycles, which can be attributed to the gradual formation of solid-electrolyte-interlayer (SEI) in initial 3 cycles (Supplementary Figs. 41 and 42)[38]. Whereas, when LiTFSI is utilized, the current intensities of all these QSS Li||Fe cells maintain stable from the 1st cycle, indicating a quicker formation of a stable SEI layer with Li-metal (Supplementary Figs. 43 and 44)[39]. In the Li||Li symmetric cells, consistent phenomena were also observed, where the overpotentials of Li-plating/stripping in all seven QSSEs with $LiPF_6$ gradually decrease in the initial 50–100 hours and then maintain stable in following 3000 hours, proving the interfacial reaction in initial section (Fig. 6c and Supplementary Figs. 45 and 46). By contrast, the voltages of these QSSEs with LiTFSI remain stable from the beginning, which is in agreement with the CV scanning (Supplementary Figs. 47 and 48). These features are also certified by the Li-deposition morphology, where more uniform and denser Li-deposition is observed when LiTFSI is employed as the salt (Supplementary Fig. 49). The Tafel plots obtained in Li||Li cells show that P(AEEO) owns higher exchange current density (j_0) than P(DOA), implying faster de-solvation kinetics of P(AEEO) based QSSE, consistent with a relatively weaker solvation ability of P(AEEO) with Li^+ and a higher Li^+-conductivity of P(AEEO) (Fig. 4 and Supplementary Figs. 50 and 51)[40,41]. It should also be noted that although $LiPF_6$ containing QSSEs are accompanied by a slightly heavier interfacial reaction with Li-metal in the initial passivation process, long stable Li plating/stripping is obtained. To lower the production cost and be closer to the current assembly line of cells, the $LiPF_6$-containing QSSEs were employed for the following cell assembly and test. From the comparison of SEM images of Li-foil after Li plating/stripping in Li||Li symmetric cells, more uniform Li-deposition is observed from the QSSEs-based cells, indicating the QSSEs successfully alleviate the interfacial reaction (Supplementary Fig. 49). In addition, the time-of-flight secondary ion mass spectroscopy (ToF-SIMS) of Li-metal after Li plating/stripping gives more obvious evidence. The Li-foil in Li|liquid-electrolyte|Li symmetric cells after Li plating/stripping show an over 85 nm thick SEI layer mainly composed of organic CH_2O-Li and CH_3O-Li, together with a thin layer of LiF (Fig. 6d and Supplementary Fig. 52). Whereas the Li-foil in Li|QSSE|Li after Li plating/stripping shows a thinner SEI layer of around 40 nm, including a layer of 20 nm organic species and a coexisting 40 nm LiF layer, indicating the interfacial reaction of organic solvents with Li-foil was significantly mitigated by QSSEs, benefiting the long-term stable cycling of the QSSE-contained cells.

In QSSEs, polymers involve the Li^+ solvation shell, and the number of solvents is reduced in Li^+ solvation structure (Fig. 4), which lowers the Li^+-migration speed, but on the other hand, suppresses the

https://doi.org/10.1038/s41467-025-59020-w

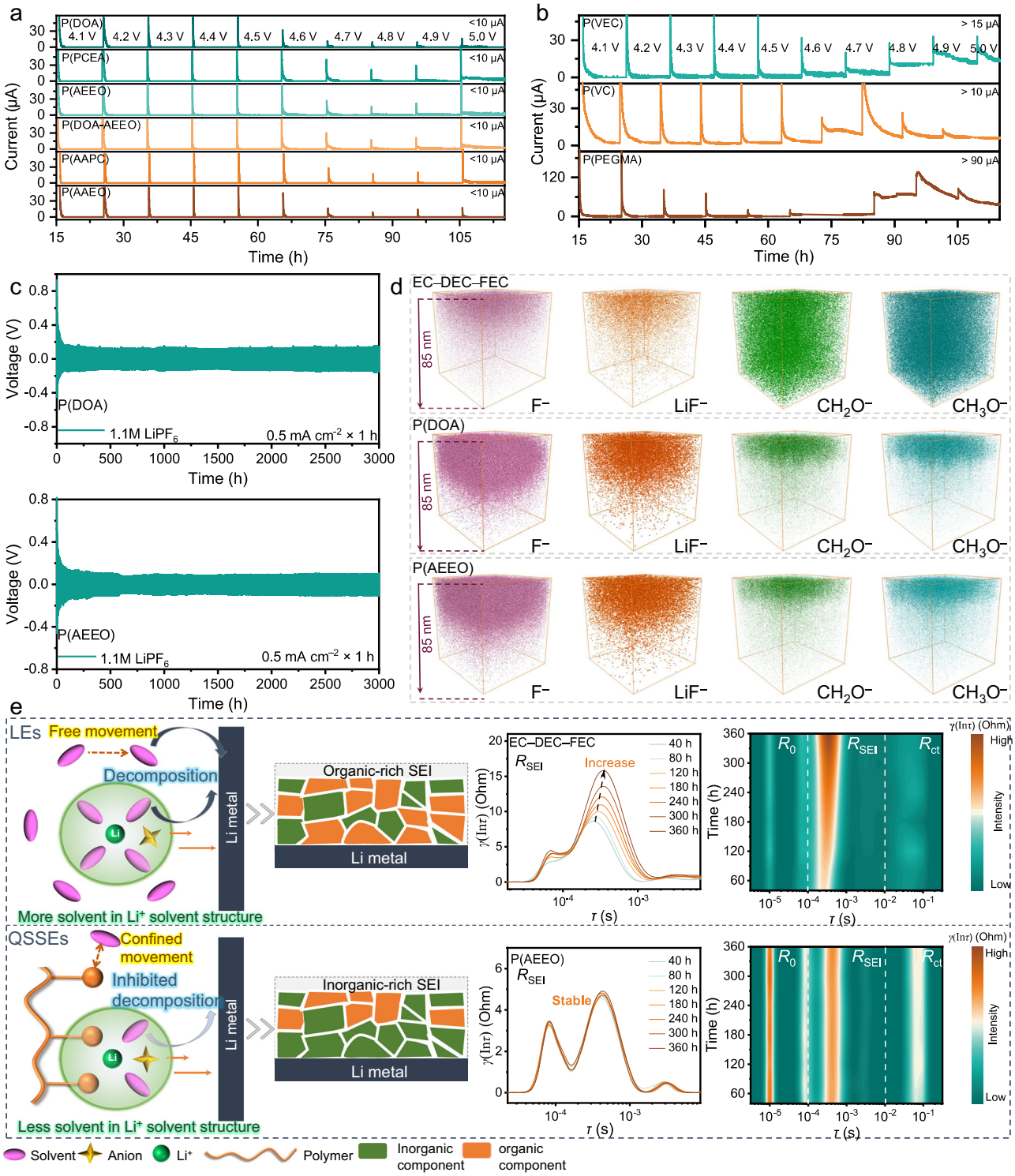

Fig. 6 | Electrochemical properties of QSSEs. a–b Electrochemical floating test of different polymers based QSSEs using NCM85 positive electrode at 25 ± 1 °C. **c** Charge-discharge profiles of the Li||Li cells with P(DOA) and P(AEEO)-based QSSEs at the current of 0.5 mA cm^{-2}, the areal capacity of 0.5 mAh cm^{-2} in each Li plating/stripping and 25 ± 1 °C. **d** The 3D mapping of CH_2O^-, CH_3O^-, F^-, and LiF^- in the ToF-SIMS sputtering volumes of the Li-foil surface after 20 times Li plating/stripping in the Li||Li cells using EC-DEC-FEC liquid electrolyte, P(DOA) and P(AEEO)-based QSSEs containing EC-DEC-FEC at the current of 0.5 mA cm^{-2}, the areal capacity of 0.5 mAh cm^{-2}, and 25 ± 1 °C. **e** Schematic of potential interfacial degradation pathways of LEs and QSSEs, and the DRT (Distribution of relaxation times) transition result of impedance curves recorded during different time (from 0 to 360 hours) Li plating/stripping in Li||Li cells at 0.5 mA cm^{-2}, 0.5 mAh cm^{-2}, and 25 ± 1 °C, R_0 as contact resistance (the τ is in the range of 10^{-6} to 10^{-4}), R_{SEI} as the resistance of Li^+ transport through the SEI (the τ is in the range of 10^{-2} to 10^{-4}) and R_{ct} as charge transfer resistance (the τ is in the range of 10^{1} to 10^{-2}).

https://doi.org/10.1038/s41467-025-59020-w

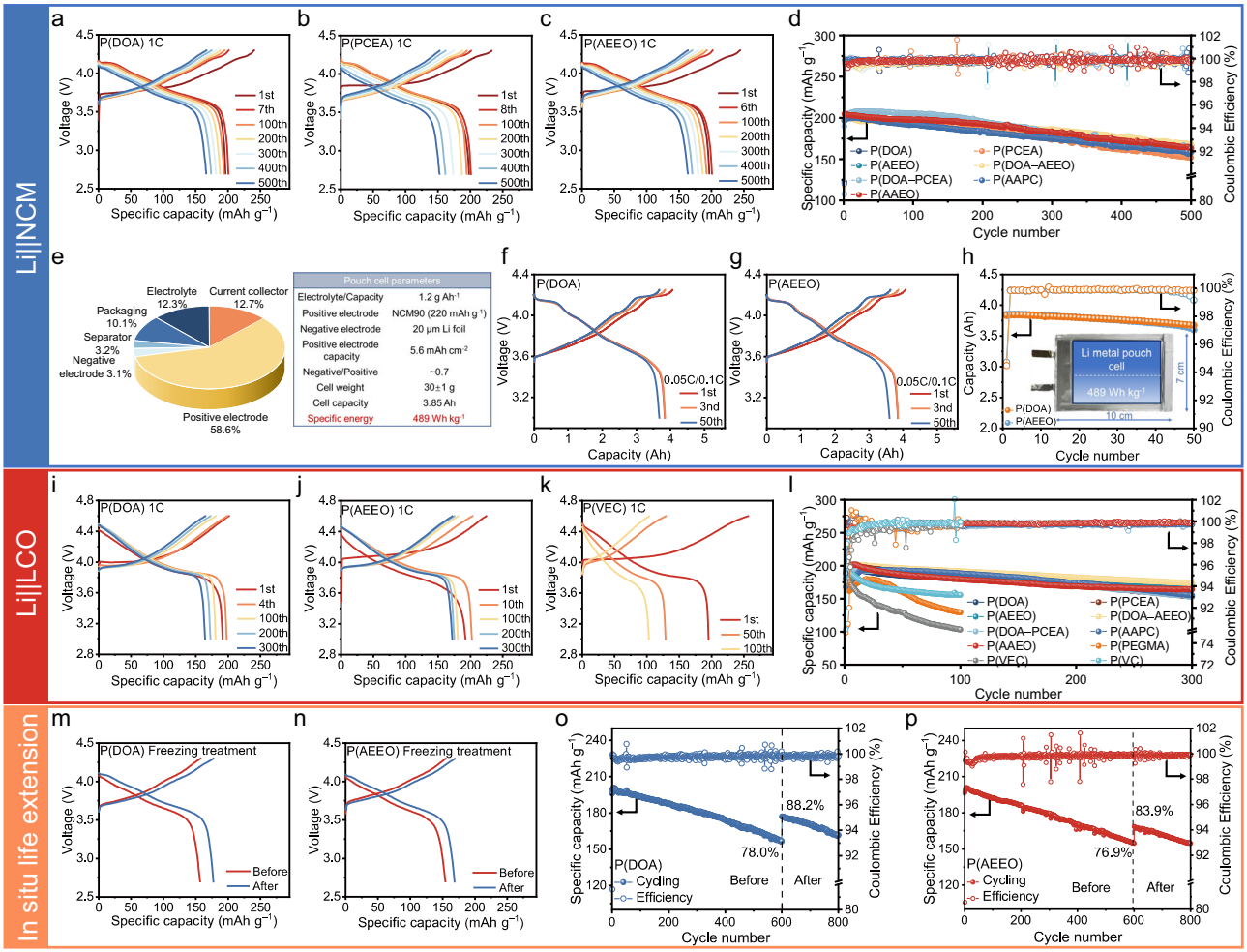

Fig. 7 | Cell performances of high-voltage QSS Li-metal cells. a–d Charge-discharge profiles and cycling performance of Li||NCM85 cells with different QSSEs at 1 C (1 C = 200 mA/g, 0.40 mA cm^{-2}) and 25 ± 1 °C. **e** Weight distribution of pouch cell components and cell design of the 489 Wh kg^{-1} pouch cell. **f–h** Charge-discharge profiles and cycling performance of 489 Wh kg^{-1} pouch cell at 0.05 C charge/0.1 C discharge (0.05 C = 11 mA/g, 0.1 C = 22 mA/g) at 25 ± 1 °C. **i–l** Charge-discharge profiles and cycling performance of Li||LCO cells with different QSSEs at 1 C (1 C = 220 mA/g, 0.44 mA cm^{-2}) and 25 ± 1 °C. **m–p** In situ life extension of QSSE Li||NCM85 cells before and after freeze at −50 °C for 12 hours, with these cells cycled at 1 C (1 C = 200 mA/g, 0.40 mA cm^{-2}) and 25 ± 1 °C. In these QSSEs, the mixed solvents of EC-DEC-FEC (2:1:1) are contained with the polymers, accounting for 30 wt%.

interfacial reaction with Li-metal owing to the reduced solvent during interfacial Li^+ de-solvation (Fig. 6e). In addition, the anion:solvent ratio on interface is higher in QSSEs, facilitating the formation of inorganic rich SEI layer and suppression of interfacial reactions, since inorganic SEI owns higher mechanical stability and better capability on interfacial passivation. To further investigate the reactions of the solvent and the negative electrode, the interfacial resistances of Li/electrolyte were in situ monitored and compared, and the DRT method was employed to assign the detailed electrochemical process in impedance curves and monitor the corresponding changes. The resistance of SEI (R_{SEI}) in Li|liquid electrolyte (LE)|Li cell is higher than that of Li|QSSE|Li cell (Fig. 6e and Supplementary Fig. 53), indicating reduced interfacial reaction of QSSE with Li-foil. In addition, with the Li plating/stripping of Li||Li cell, R_{SEI} of the Li||Li cell with LE undergoes a heavier increase than that of the Li|QSSE|Li, verifying that the QSSEs are effective in inhibiting the interfacial reaction by anchoring solvent molecules (Supplementary Note 1).

Cell performance and the in situ non-destructive life extension of QSS cells

Since high nickel NCM is currently the most dominant positive electrode owing to the high energy density[42], the QSS Li||NCM85 cells were fabricated by in situ polymerization and employed to evaluate the performance of these QSSEs. After the in situ polymerization, the internal pores among positive electrode particles were filled with QSSEs, which were directly observed by SEM and the polymers were rinsed out for ^{1}H NMR test, showing over 99% conversion rates without obvious residual double bonds (Supplementary Figs. 54–57), similar to the in situ polymerization in PP separator, benefiting to the improvement of antioxidation capability. Typical charge-discharge voltage profiles of NCM85 were observed (Fig. 7a–d), with the initial discharge capacities of 196.2, 198.0, 196.7, 198.0, 190.0, 198.0 and 204.8 mAh g^{-1} at 1 C for P(DOA), P(PCEA), P(AEEO), P(DOA-AEEO), P(DOA-PCEA), P(AAPC) and P(AAEO) based QSSEs, and the corresponding initial Coulombic efficiencies of 81.61%, 85.16%, 80.55%, 81.31%, 80.54%, 81.45%, and 83.12% (Supplementary Fig. 58), respectively, which are similar to traditional liquid electrolytes, indicating the successful construction of QSS Li||NCM85 cells. After 500 cycles, the capacity retentions of 83–75% are obtained (Fig. 7d). P(DOA-AEEO) delivered the highest capacity retention of 83.9%, followed by P(DOA), P(AEEO), P(AAEO), P(AAPC), and then the copolymer of P(DOA-PCEA). Among these QSS cells, P(PCEA) gave a relatively poor capacity retention of 75.8%, slightly worse than the others. In higher positive electrode loading of over 3 mAh cm^{-2}, stable cycling performance could still be

obtained (Supplementary Fig. 59 and Supplementary Note 2), indicating the successful suppression of interfacial reaction with Li-metal negative electrode through confining liquid electrolytes. In larger pouch cells assembled with NCM90 ($LiNi_{0.9}Co_{0.05}Mn_{0.05}$ with the gram capacity of 220 mAh g^{-1}) as positive electrode and double-side 20 µm Li on copper foil as negative electrode, the QSSEs of P(DOA) and P(AEEO) are in situ polymerized under lean electrolyte conditions of Electrolyte/Capacity = 1.2 g Ah^{-1} (Fig. 7e and Supplementary Fig. 60). These cells deliver the specific energy of 489 Wh kg^{-1} with a high energy retention of 93-96% after 50 cycles (Fig. 7f–h), implying the promising potentiality of these QSSEs used in high-energy Li-metal batteries.

High voltage LCO with the cutting off voltage at 4.6 V is desired for 3C electronic devices, whose long-life cycling requires not only the suppression of structure collapse of LCO, but also the alleviation of interfacial reactions of electrolyte with delithiated LCO at over 4.4 V[43–46]. In QSSEs, the diffusion of liquid electrolyte is largely suppressed, which is beneficial for inhibiting the interfacial reactions with liquid electrolyte. As shown in Fig. 7i–l and Supplementary Fig. 61, the QSS Li||LCO cells fabricated with these seven QSSEs give characteristic charge-discharge voltage profiles of LCO, showing the discharge capacity of around 200 mAh g^{-1} at the cutoff voltage of 4.6 V. After 300 cycles, the capacity retentions of these QSSEs-based cells are in the range of 86–77%. Similar to the above QSS Li||NCM85 cells, there is no significant difference in the cycling stability of these seven QSSEs. It is worth noting that the cycling performance of all seven QSS Li||LCO cells is better than that of using liquid EC-DEC-FEC (2:1:1 with 1.1 M $LiPF_6$) (Supplementary Fig. 62), indicating the advantage of QSSEs with the capability of suppressing interfacial reactions. On the contrary, the Li||LCO cells using the in situ polymerized QSSEs of VEC, VC, and PEGMA only show capacity retentions of 52.9%, 81.0%, and 66.8% after 100 cycles (Fig. 7k, l and Supplementary Fig. 61), respectively, which are significantly worse than the cells fabricated with P(DOA), P(PCEA), P(AEEO), P(AAPC), P(AAEO), and their copolymer-based QSSEs. For VEC and VC, although they can be in situ polymerized in liquid electrolytes, the polymerization degrees of both monomers are only in the range of 50–80%, which means there are still 20–50% residual monomers[18,19]. Since both monomers contain double-bonds and the double-bonds could be electrochemically oxidized at 4.3-4.5 V, which would deteriorate the cycling performance. While for PEGMA, although the polymerization degree is near 100%, the presence of ether units in PEGMA leads to poor stability at higher than 4.0 V. In addition, the higher voltage QSS Li|P(AEEO)|LRMO cell also showed stable cycling with the capacity of over 215 mAh g^{-1} at the cutting off charge voltage of 4.8 V and 0.2 C (Supplementary Fig. 63). After 100 cycles, the capacity retention is 91.3%, indicating the remarkably high-voltage stability of P(AEEO)-based QSSE. These results verify that these ether-free and high polymerization degree polymers possess the desired high voltage stability and the success of molecular design.

It should be noted that the cycling performance of these QSSE-based Li||NCM85 cells still does not meet the market required life for commercial batteries, which can be attributed to the gradual depletion of liquid electrolytes on the interface of Li-metal/QSSE, since the confined liquid electrolyte in QSSEs can't diffuse quickly or re-wet the interface timely manner, although ~54 wt% liquid solvent is confined in these QSSEs. As discussed above, the freezing treatment of QSSEs would lead to the crystallization of polymer in QSSEs and the subsequent release of confined liquid solvent, which should re-wet the interface with Li-metal. After warming to room temperature, the amorphous polymer would be regenerated and reabsorb liquid, recovering homogeneous QSSEs and rebuilding the interface with Li-metal. As shown in Fig. 7m–p, the P(DOA) and P(AEEO) based QSS Li||NCM85 cells maintain the capacity retentions of 78.0% and 76.9% after 600 cycles, respectively, which were cooled to −50 °C for 12 hours and then naturally warmed to room temperature. After that, the cell delivered capacity retentions of 88.2% and 83.9% for P(DOA) and P(AEEO) contained Li||NCM85 cells, indicating 10–7% capacity is recovered after this freezing treatment (Supplementary Fig. 64). Both cells run stably and give the capacity retention of 77-80% after additional 200 cycles, indicating this freezing treatment successfully extend the cycling life and renew the cells around 1/3. This life-extension strategy does not need to damage the cell package and so eliminates the safety risk[47]. In addition, this process only involves physical crystallization and de-crystallization, and does not involve any chemical reaction on QSSE or high temperature heat treatment, maintaining well the chemical structure of polymers and thermally sensitive $LiPF_6$. These features demonstrate the feasibility of constructing in situ life-prolongable QSSE-based solid-state batteries.

Discussion

These acrylate-based ether-free monomers containing Li^+-ligands were designed and prepared, which show ~100% polymerization degree in the presence of Li-metal and positive electrodes, possessing high antioxidation capability. In addition, these polymers own strong solvent absorption capability, showing solid-state even when absorbing 54 wt% liquid solvent. From the detailed studies on ^1H NMR, FT-IR, MD, and DFT simulation, it is demonstrated that higher polymer-solvent affinity and stronger coordination of liquid solvent with Li^+ but weaker polymer-Li^+ coordination capability, are all beneficial to the Li^+-migration. A poor polymer-solvent affinity easily leads to the micro phase-separation and generates interphase barriers of Li^+ movement, owing to the sharp difference in the Li^+-conductivity between dry polymer and liquid. Higher polymer-solvent affinity facilitates the formation of a homogeneous polymer-solvent composite without an interphase gap, benefiting the Li^+ transport. In QSSEs, the solvation capability of solvent and polymer shows an opposite effect for the Li^+-conductivity: a stronger solvation capability of liquid solvent is beneficial to the Li^+-migration, but a weaker solvation capability of solid polymer is helpful for Li^+-transport, since polymer could not move with the migration of Li^+ but liquid solvent molecules migrate with Li^+. Owing to better affinity with polymers and higher solvation capability of EC, the EC-containing QSSEs show higher Li^+-conductivity. With the same solvent, oxalate-based polymers deliver higher Li^+-conductivity than carbonyl-based polymers since the Li^+ de-solvation energy is lower for oxalate.

These acrylate-based ether-free polymers show high oxidation voltage to 5.0 V, endowing the long-term stable cycling of QSS Li||LCO and Li||LRMO cells to 4.8 V. Whereas, the traditionally used VEC and VC own lower polymerization degrees of 50–80% with 20–50% residual double-bonds containing monomers, which tend to be oxidized at 4.3-4.5 V and cause a poor cycling stability of 4.6 V Li||LCO cells. It should be noted that the confinement of liquid in QSSEs presents a dual-edged characteristic, which alleviates the interfacial reactions to a large extent, but suppresses the liquid diffusion to wet the interface in a timely manner. Through the freezing treatment of QSSE-based cells, the polymers crystallize, and the absorbed liquid is released to re-wet the interface with Li-metal. After warming up to room temperature, the homogeneous QSSEs are regenerated and the Li^+-conductive interface is rebuilt, which partially recovers the capacity and extends the cycling life of cells. Since this process does not involve any cell disassembly, chemical reaction, or high temperature treatment, this reversible low-temperature crystallization of polymer-based QSSEs gives a safe way for the development of non-destructively life extendable batteries and supercapacitors.

Methods

Synthesis of ether-free acrylate/acrylamide monomers

DOA monomer: GC (4-(hydroxymethyl)-1,3-dioxolan-2-one, 90% purity) (20.0 g, 169.5 mmol), NEt_3 (triethylamine, 99% purity) (18.9 g, 186.4 mmol) and anhydrous DCM (dichloromethane, 99.9% purity)

(160 mL) were added to three-necked round flask (500 mL), and then the reaction mixture was stirred at 0 °C for 20 minutes under N_2 (nitrogen) flow. AC (acryloyl chloride, 96% purity) (16.5 g, 186.4 mmol) was dissolved in anhydrous DCM (60 mL), which was then added to the above reaction mixture dropwise. After the AC solution was added, the reaction solution was returned to 25 °C and kept at 25 °C for 8 hours under N_2 flow. The solution was washed with distilled water (3 × 150 mL), and then the solvent was evaporated to generate the crude product, which was purified by silica gel column chromatography, giving a colorless oil (21.9 g, 75%).

AEEO monomer: HEA (hydroxyethyl acrylate, 96% purity) (20.0 g, 172.2 mmol), Py (pyridine, 99.9% purity) (15.0 g, 189.4 mmol) and anhydrous DCM (160 mL) were added to three-necked round bottom flask (500 mL), and then the reaction mixture was stirred at 0 °C for 20 minutes under N_2 flow. EOM (ethyl oxalyl monochloride, 98% purity) (25.9 g, 189.4 mmol) was dissolved in anhydrous DCM (60 mL), which was then added to the above reaction mixture dropwise. After the EOM solution was added, the reaction solution was returned to 25 °C and kept at 25 °C for 4 hours under N_2 flow. The solution was washed with distilled water (3 × 150 mL), and then the solvent was evaporated to generate the crude product, which was purified by silica gel column chromatography, giving a colorless oil (29.9 g, 80%).

The other monomers were prepared following the above procedure and purified using silica gel column chromatography, with a yield of 80-88%.

The raw materials for the preparation of the above monomer were bought from Aladdin.

Preparation of QSS electrolytes

Preparation of QSSE electrolytes: The DOA monomer (3 g), EC (ethylene carbonate, ≥99% purity) (2.7 g), DEC (diethyl carbonate, ≥99% purity) (1.35 g), FEC (fluoroethylene carbonate, ≥99% purity) (1.35 g), $LiPF_6$ (lithium hexafluorophosphate, ≥99.99% purity) (1.6 g) were added to the vial and stirred at 25 °C. After that, AIBN (azobisisobutyronitrile, ≥99% purity) (0.025 g, 0.3 wt% relative to the whole mixture) was added to the vial and stirred as the precursor solutions. The precursor solutions were heated to 55 °C for 1 hour and then 45 °C for 12 hours to obtain QSSE, in which the weight ratios of polymer, liquid solvent, and $LiPF_6$ are 30 wt%, 54 wt%, and 16 wt%, respectively.

Self-standing P(DOA) QSSE membrane: The DOA precursor solution with EC-DEC-FEC (2:1:1, weight ratio) and AIBN was stirred at 55 °C for 15 minutes. After that, the viscous solution was poured into a glass mold, which was then sealed with 3 M tape to prevent solvent evaporation. The mode was placed in an oven and heated to 55 °C for 45 minutes, and then 45 °C for 12 hours to give the DOA-based QSSE membrane. The solvents of EC, DEC, FEC, and $LiPF_6$ were purchased from Sigma-Aldrich. AIBN was purchased from Aladdin.

PP separator coating: The precursor solution was infiltrated into a porous PP separator, after that the separator was placed into a PP petri dish, which was sealed with 3 M tape to prevent solvent evaporation. The petri dish was then put into an oven and heated to 55 °C for 1 hour, followed by an additional 12 hours at 45 °C to ensure complete reaction and give the QSSE coating on the PP separator. The PP separator was supplied by Hefei Solarton New Material Technology Co. Ltd. and has a thickness of 15 ± 2.0 μm, a porosity of 60 ± 5%, and an average pore size of 80 nm.

The above processes were conducted in an argon-filled glovebox (H_2O < 0.1 ppm, O_2 < 0.1 ppm) at 25 ± 5 °C.

Synthesis of $LiCoO_2$ material

The LCO material was prepared via the high-temperature solid-state sintering method, utilizing precursor materials of Li_2CO_3 (≥99% purity), Co_3O_4 (99.9% purity), Al_2O_3 (≥99.9% purity), MgO (≥98% purity), and TiO_2 (≥99.9% purity). To compensate for the lithium loss during the high-temperature calcination process, an excess of 5 wt% Li_2CO_3 was used. The precursor materials were mixed and ground in an agate mortar, followed by sintering in an alumina crucible at 1000 °C for 10 hours to form the intermediate product. The intermediate product was then reground in the agate mortar and subsequently sintered a second time at 900 °C for 10 hours to obtain the final product[43]. The above materials were bought from Aladdin.

Preparation of positive electrodes and QSS cell assembly

The preparation of positive electrodes: for coin cells, the positive electrode material of NCM85 or LCO or LRMO, conductive carbon black and PVDF (poly(vinylidene fluoride)) in the ratio of 80:10:10 was mixed in NMP (N-methyl-2-pyrrolidone, 99.9% purity) to give a homogeneous slurry, which was single-side coated on Al (aluminum) foil in two loadings of 2 and 15 mg cm^{-2}. The electrode films were vacuum dried at 60 °C for 24 hours and then cut into 12 mm diameter discs before being used in cell fabrication.

For pouch cells, the positive electrode material of NCM90, PVDF, Super P (TIMREX KS-6) and single-walled carbon nanotubes (CNT) in the weight ratio of 96:2:1:1 was mixed in NMP to give a homogeneous slurry, which was double-sided coated on Al foil. The electrode films were vacuum dried at 100 °C for 24 hours and then cut into 55 mm × 77 mm before using in cell fabrication.

The doctor blade (KTQ-80 F) and precision disc cutting machine (MSJ-T10) for coin cells were bought from Shenzhen Kejing Star Technology Co. Ltd. The automatic coating machine and slitting machine for pouch cells were from Guangzhou CLG Electric Equipment Co. Ltd. and Beijing Sevenstar Electronics Co. Ltd. NCM85 was bought from Global Battery Materials BASF (China) Co. Ltd. NCM90 and LRMO were bought from China Automotive Battery Research Institute Co. Ltd. and PVDF was bought from Arkema. The Al foil was bought from Shenzhen Kejing Star Technology Co. Ltd. NMP was bought from Aladdin. The Super P and CNT were bought from TIMCAL and Bertrand. Unless otherwise stated, the purity of the raw materials is battery grade.

The above preparation of positive electrodes was carried out in drying room (−40 °C dew point temperature) at 25 ± 5 °C.

QSS cell assembly

The preparation of precursor solutions: the mixed solvent of EC-DEC-FEC (2:1:1), $LiPF_6$, and different monomers (DOA, PCEA, AEEO, AAPC, AAEO) was added to the vial and stirred at 25 °C, followed by the addition of 0.3–0.5 wt% AIBN, which is the precursor solution. When DOA is copolymerized with PCEA or AEEO, the mole ratio of DOA to PCEA or AEEO is constant at 1:1, and the concentration of $LiPF_6$ is maintained at 1.1 M (about 16 wt%), with the liquid solvents accounting for ~54 wt%. The preparation of precursor solutions was made in an argon-filled glovebox (H_2O < 0.1 ppm, O_2 < 0.1 ppm) at 25 ± 5 °C.

Coin cells assembly: The coin cells were made with NCM85/LCO/LRMO positive electrode and Li metal negative electrode (15.6 mm diameter × 0.45 mm thickness, ≥99.9% purity) using 2032 SS cases with a sealing pressure of 0.50 MPa. Each cell injects 1.5 ± 0.1 mg (corresponding to the positive electrode loading of 2 mg cm^{-2}) or 10.5 mg (corresponding to the positive electrode loading of 15 mg cm^{-2}) of precursor solutions. After precursor solutions were injected into cells, the cells were kept at 4 °C fridge for 24 hours for full infiltration of liquid. After that, the cells were placed in 55 °C oven for 4 hours and then maintained at 45 °C for 12 hours. The above coin cells were assembled in an argon-filled glovebox (H_2O < 0.1 ppm, O_2 < 0.1 ppm) at 25 ± 5 °C.

Pouch cells assembly: The pouch cells were made NCM90 positive electrode and Li metal negative electrode. The pouch cell comprised 10 double-side positive electrodes (55 mm × 77 mm) and 11 double-side negative electrodes (double-side 20 μm Li on 8 μm Cu (copper) foil, 57 mm × 77 mm), in which PP separator was wrapped around the electrodes to prevent short circuits, stacked in a drying chamber

(−40 °C dew point temperature) at 25 ± 5 °C. Each pouch cell was injected with 3.4 g precursor solutions and then vacuum encapsulated. The cell stayed at 4 °C fridges for 24 hours for full infiltration of liquid. After that, the cells were placed in 55 °C oven for 4 hours and then maintained at 45 °C for 12 hours. Pre-charging was followed by cutting off the air pocket and sealing it again to get rid of gas at −95 Kpa. The pouch cell was cycling at 0.1 MPa pressure by SS plates.

The 2032/304 SS was supplied by Shenzhen Kejing Star Technology Co. Ltd., and Li metal and Li-Cu composite tape were supplied by China Energy Lithium Co., Ltd.

Electrochemical measurements

All cells used for electrochemical characterization were kept at a temperature of 25 ± 1 °C in a constant temperature chamber (Shanghai BOLAB Equipment Co., BLC-300). Unless otherwise specified, all tests were carried out at 25 ± 1 °C.

The electrochemical floating test was performed on the LAND battery test system (CT3002A, Wuhan, China) at 25 ± 1 °C. In this test, the Li||NCM cells were first charged to 4.0 V and then were applied a constant voltage charge from 4.1 to 5 V, for 10 hours in each held voltage.

The galvanostatic charge-discharge tests of the coin cells of Li||Li, Li||NCM85, Li||LRMO, and Li||LCO were performed on the LAND battery test system (CT3002A, Wuhan, China) at a temperature of 25 ± 1°C. The Li||Li cells were tested at an areal capacity of 0.5 mAh cm^{-2} for each Li plating/stripping. The Li||NCM85, Li||LCO, and Li||LRMO cells were charged and discharged within the voltage ranges of 2.7–4.3 V, 3–4.6 V, and 2–4.8 V, respectively. The Li||NCM85 cells were cycled at a current density of 1 C or 0.2 C, the Li||LCO cells were cycled at a current density of 1 C, and the Li||LRMO cells were cycled at a current density of 0.2 C.

The galvanostatic charge/discharge tests of pouch cells were performed on the LAND battery test system (CT3002A, Wuhan, China) at 25 ± 1 °C. The pouch cells were charged and discharged within a voltage range of 3-4.25 V and cycled at a current density of 0.05 C in charge process and 0.1 C in discharge process.

The ionic conductivities of QSSEs at various temperatures (ranging from 25 to 70 °C) were measured using electrochemical impedance spectroscopy (EIS). This assessment was conducted at a frequency range of 1.0 MHz to 1.0 Hz on a Solartron Analytical cell test system with an amplitude of 10 mV, in which the EIS adopted potentiostatic (0 V *vs* OCV) with the number of 12 data points of per decade of frequency and 10 seconds for open-circuit voltage time applied before performing the EIS measurement, employing SS as electrodes in coin type cell of SS|QSSEs|SS. The ionic conductivities were calculated using the following method:

$$\sigma = L/RS \tag{1}$$

Here, L represents the thickness of the QSSE membranes, R denotes the resistance of the bulk electrolyte, and S signifies the effective contact area between the electrolyte and solid-state electrodes.

The cyclic voltammetry (CV) plots for Li||SS cells were measured using a Solartron Analytical at 25 ± 1 °C. The first cycle was scanned from OCV (open-circuit voltage) to −0.5 V, followed by a positive scan from −0.5 V to 1 V. Subsequent cycles were scanned from 1 V to −0.5 V, and then back from −0.5 V to 1 V, maintaining a constant scanning rate of 0.2 mV s^{-1}.

Characterizations

The GPC measurements were carried out using a Waters GPC 1515 at a temperature of 25 °C. The ^{1}H NMR and ^{7}Li NMR measurements were conducted using a Bruker AVANCE III 400 MHz spectrometer at 25 °C.

The single crystals of AAEO were analyzed using a single-crystal x-ray diffraction (SXRD, Gemin E). The FT-IR spectra were obtained by the attenuated total reflection method with a Nicolet 6700 FT-IR spectrometer. The WAXS (wide-angle X-ray scattering) spectra were detected by a Xeuss 2.0 (Xenocs). The XRD (X-ray diffraction) spectra were detected by D8 Discover (Bruker) with Cu Ka radiation in the scan range of 10–70° and a speed of 2° min^{-1}. The differential scanning calorimetry (DSC, NETZSCH DSC 214 Polyma) analysis was conducted at a heating rate of 20 °C min^{-1} under a nitrogen atmosphere. The thermogravimetric analysis (TGA, NETZSCH TG209F3) test was conducted at a scan rate of 10 °C min^{-1} under an argon atmosphere from 40 to 600 °C. All samples for the above tests were prepared and sealed in an argon-filled case within an argon-filled glovebox (H_2O < 0.1 ppm, O_2 < 0.1 ppm).

A JSM-7800 field emission scanning electron microscope (SEM) was used to observe the morphology of the PP separator and positive electrode after in situ polymerized QSSEs and the Li-foil electrode after Li plating/stripping. Time-of-flight secondary ion mass spectrometry (ToF-SIMS) was utilized to characterize the SEI composition on the Li metal electrode after Li plating/stripping by FIB-SEM-TOF-SIMS (TESCAN Brno, s. r. o.). The experimental setup involved a pulsed 30 keV gallium ion beam, with the selected analysis region of 100 × 100 µm. Post-cycling cells were disassembled in an argon-filled glovebox (H_2O < 0.1 ppm, O_2 < 0.1 ppm), followed by the sample preparation for SEM and ToF-SIMS analysis. The samples were placed into an argon-filled case for further testing.

Calculation of battery-specific energy

Battery specific energy refers to the amount of energy (Wh) that a battery can release per unit mass (kg). It is calculated using the formula:

$$\text{Battery specific energy (Wh kg}^{-1}\text{)} = \text{Discharge energy (Wh)}/\text{Battery mass (kg)} \tag{2}$$

In this study, the specific energy of the pouch cell was found to be 489 Wh kg^{-1}. This value was calculated based on a discharge capacity of 3.85 Ah and an energy of 14.73 Wh, with the battery mass of 30.12 g.

Computational methods

Molecular dynamics (MD) simulations were performed using GROMACS code[48]. The Optimized Potentials for Liquid Simulations All Atom force fields parameters and the Restrained ElectroStatic Potential charges from Multiwfn were used for EC, DEC, and polymer chains[49–51]. To simplify the model, six repeating monomers of P(DOA) and P(AEEO), were used to represent the corresponding polymers. In calculation box, 20 polymer segments (each segment contains 6 repeated monomers), 360 solvent molecules, and 60 $LiPF_6$ are included. The force fields of polymers and solvents are generated using LigParGen software, which allows a maximum ligand size of 200 atoms. The force field for PF_6^- was accessed from a previous study[52]. The initial simulation boxes were created using the PACKMOL software[53]. Sequential MD simulations were performed under different ensembles. An isothermal-isobaric ensemble protocol was initially implemented at 600 K for a duration of 5 ns. This was followed by an extended equilibration period at 298 K for 10 ns. Subsequently, the system was transitioned to a canonical (NVT) ensemble configuration maintained at 298 K for an additional 10 ns duration. The structure of the electrolyte system was derived from trajectory analysis of the terminal 5 ns segment in the NVT. In this context, *N* refers to the fixed number of particles, *P* denotes the system pressure, *T* represents the temperature, and *V* defines the system volume.

For further exploration of the interaction between polymer, solvent, and Li^+, the de-solvation energy of Li^+-solvent-polymer complexes was investigated by density functional theory (DFT), in which the Li^+ solvated structures were extracted from MD simulations. All quantum chemical calculations were performed using ORCA (version

5.0.3)[54–56]. All geometry optimizations have been optimized at the B3LYP-D3/def2-TZVP level[57]. The precise single-point energy was obtained by wB97M-V with the def2-TZVPP basis set. Optimized chemical structures of various Li^+-solvent-polymer complexes were visualized by VESTA[58]. The binding energy (ΔE) is calculated using the following equation:

$$\Delta E = E_{ALi} - E_A - E_{Li} \quad (3)$$

Here, E_{ALi}, E_A, and E_{Li} are the total energy of polymer-solvent-Li^+ complexes, energy of polymer-solvent complexes, and energy of Li^+ alone. The de-solvation energy was defined as follows:

$$-\Delta E = E_A + E_{Li} - E_{ALi} \quad (4)$$

The employed MD and DFT structures can be seen in Supplementary Data 1–18.

Data availability

The crystallographic data of AAEO have been deposited in the Cambridge Crystallographic Data Centre database under accession code CCDC 2354001 https://www.ccdc.cam.ac.uk/structures/. The other relevant data generated in this study are provided in the Supplementary Information/Source Data file. Source data are provided with this paper.

References

1. Etacheri, V., Marom, R., Elazari, R., Salitra, G. & Aurbach, D. Challenges in the development of advanced Li-ion batteries: a review. *Energy Environ. Sci.* **4**, 3243–3262 (2011).
2. Liu, K., Liu, Y., Lin, D., Pei, A. & Cui, Y. Materials for lithium-ion battery safety. *Sci. Adv.* **4**, eaas9820 (2018).
3. Liu, J. et al. Pathways for practical high-energy long-cycling lithium metal batteries. *Nat. Energy* **4**, 180–186 (2019).
4. Cheng, X.-B., Zhang, R., Zhao, C.-Z. & Zhang, Q. Toward safe lithium metal anode in rechargeable batteries: a review. *Chem. Rev.* **117**, 10403–10473 (2017).
5. Janek, J. & Zeier, W. G. A solid future for battery development. *Nat. Energy* **1**, 16141 (2016).
6. Manthiram, A., Yu, X. & Wang, S. Lithium battery chemistries enabled by solid-state electrolytes. *Nat. Rev. Mater.* **2**, 16103 (2017).
7. Fan, L.-Z., He, H. & Nan, C.-W. Tailoring inorganic-polymer composites for the mass production of solid-state batteries. *Nat. Rev. Mater.* **6**, 1003–1019 (2021).
8. Wang, Z.-Y. et al. Achieving high-energy and high-safety lithium metal batteries with high-voltage-stable solid electrolytes. *Matter* **6**, 1096–1124 (2023).
9. Mindemark, J., Lacey, M. J., Bowden, T. & Brandell, D. Beyond PEO-alternative host materials for Li^+-conducting solid polymer electrolytes. *Prog. Polym. Sci.* **81**, 114–143 (2018).
10. Zhou, Q., Ma, J., Dong, S., Li, X. & Cui, G. Intermolecular chemistry in solid polymer electrolytes for high-energy-density lithium batteries. *Adv. Mater.* **31**, 1902029 (2019).
11. Huo, S. et al. Challenges of polymer electrolyte with wide electrochemical window for high energy solid-state lithium batteries. *InfoMat* **5**, e12394 (2023).
12. Ding, P. et al. Polymer electrolytes and interfaces in solid-state lithium metal batteries. *Mater. Today* **51**, 449–474 (2021).
13. Yang, S.-J. et al. Intrinsically safe lithium metal batteries enabled by thermo-electrochemical compatible in situ polymerized solid-state electrolytes. *Adv. Mater.* **36**, 2405086 (2024).
14. Zhang, Q.-K. et al. Homogeneous and mechanically stable solid-electrolyte interphase enabled by trioxane-modulated electrolytes for lithium metal batteries. *Nat. Energy* **8**, 725–735 (2023).
15. Zou, S. et al. In situ polymerization of solid-state polymer electrolytes for lithium metal batteries: a review. *Energy Environ. Sci.* **17**, 4426–4460 (2024).
16. Cheng, X., Pan, J., Zhao, Y., Liao, M. & Peng, H. Gel polymer electrolytes for electrochemical energy storage. *Adv. Energy Mater.* **8**, 1702184 (2018).
17. Chai, J. et al. In situ generation of poly(vinylene carbonate) based solid electrolyte with interfacial stability for $LiCoO_2$ lithium batteries. *Adv. Sci.* **4**, 1600377 (2017).
18. Lin, Z. et al. A wide-temperature superior ionic conductive polymer electrolyte for lithium metal battery. *Nano Energy* **73**, 104786 (2020).
19. Li, P. et al. Efficiencies of various in situ polymerizations of liquid electrolytes and the practical implications for quasi solid-state batteries. *Angew. Chem. Int. Ed.* **62**, e202309613 (2023).
20. Chen, K. et al. Correlating the solvating power of solvents with the strength of ion-dipole interaction in electrolytes of lithium-ion batteries. *Angew. Chem. Int. Ed.* **62**, e202312373 (2023).
21. Xie, X. et al. Rational design of F-modified polyester electrolytes for sustainable all-solid-state lithium metal batteries. *J. Am. Chem. Soc.* **146**, 5940–5951 (2024).
22. Tang, L. et al. Polyfluorinated crosslinker-based solid polymer electrolytes for long-cycling 4.5 V lithium metal batteries. *Nat. Commun.* **14**, 2301 (2023).
23. Wang, C. et al. High polymerization conversion and stable high-voltage chemistry underpinning an in situ formed solid electrolyte. *Chem. Mater.* **32**, 9167–9175 (2020).
24. Wang, Y. et al. Electrolyte-mediated misconception of carbon-based electrode performance and beyond in metal-ion batteries. *Adv. Energy Mater.* **13**, 2301354 (2023).
25. Wang, Y. et al. Weak solvent-solvent interaction enables high stability of battery electrolyte. *ACS Energy Lett.* **8**, 1477–1484 (2023).
26. Su, C.-C. et al. Solvating power series of electrolyte solvents for lithium batteries. *Energy Environ. Sci.* **12**, 1249–1254 (2019).
27. Cheng, H. et al. Emerging era of electrolyte solvation structure and interfacial model in batteries. *ACS Energy Lett.* **7**, 490–513 (2022).
28. Fan, X. & Wang, C. High-voltage liquid electrolytes for Li batteries: progress and perspectives. *Chem. Soc. Rev.* **50**, 10486–10566 (2021).
29. Lu, D. et al. Ligand-channel-enabled ultrafast Li-ion conduction. *Nature* **627**, 101–107 (2024).
30. Hao, S.-M. et al. Water-in-polymer electrolyte with a wide electrochemical window and recyclability. *Nat. Sustain.* **7**, 661–671 (2024).
31. Zhang, W. et al. Single-phase local-high-concentration solid polymer electrolytes for lithium-metal batteries. *Nat. Energy* **9**, 386–400 (2024).
32. Shah, N. J. et al. Nanosecond solvation dynamics in a polymer electrolyte for lithium batteries. *Nat. Mater.* **23**, 664–669 (2024).
33. Alcock, B., Olafsen, K., Huse, J. & Grytten, F. The low temperature crystallization of hydrogenated nitrile butadiene rubber (HNBR). *Polym. Test.* **66**, 228–234 (2018).
34. Neidhart, E. K. et al. C-H Functionalization of polyolefins to access reprocessable polyolefin thermosets. *J. Am. Chem. Soc.* **145**, 27450–17458 (2023).
35. Drago, R. S., Corden, B. B. & Barnes, C. W. Novel cobalt(II)-catalyzed oxidative cleavage of a carbon-carbon double bond. *J. Am. Chem. Soc.* **108**, 2453–2454 (1986).
36. Yao, Q.-J. et al. Enantio- and regioselective electrooxidative cobalt-catalyzed C-H/N-H annulation with alkenes. *Angew. Chem. Int. Ed.* **62**, e202218533 (2023).
37. Pan, X. et al. High voltage stable polyoxalate catholyte with cathode coating for all-solid-state Li-metal/NMC622 batteries. *Adv. Energy Mater.* **10**, 2002416 (2020).
38. Aurbach, D. et al. Design of electrolyte solutions for Li and Li-ion batteries: a review. *Electrochim. Acta* **50**, 247–254 (2004).

39. Aurbach, D., Zinigrad, E., Cohen, Y. & Teller, H. A short review of failure mechanisms of lithium metal and lithiated graphite anodes in liquid electrolyte solutions. *Solid State Ion.* **148**, 405–416 (2002).
40. Zhang, Q.-K. et al. Regulating solvation structure in nonflammable amide-based electrolytes for long-cycling and safe lithium metal batteries. *Adv. Energy Mater.* **12**, 2200139 (2022).
41. Zheng, J. et al. Electrolyte additive enabled fast charging and stable cycling lithium metal batteries. *Nat. Energy* **2**, 17012 (2017).
42. Li, W., Erickson, E. M. & Manthiram, A. High-nickel layered oxide cathodes for lithium-based automotive batteries. *Nat. Energy* **5**, 26–34 (2020).
43. Zhang, J.-N. et al. Trace doping of multiple elements enables stable battery cycling of $LiCoO_2$ at 4.6 V. *Nat. Energy* **4**, 594–603 (2019).
44. Zhang, A. et al. Regulating electrode/electrolyte interfacial chemistry enables 4.6 V ultra-stable fast charging of commercial $LiCoO_2$. *Energy Environ. Sci.* **17**, 3021–3031 (2024).
45. Huang, Y. et al. Construction of sulfone-based polymer electrolyte interface enables the high cyclic stability of 4.6 V $LiCoO_2$ cathode by in situ polymerization. *Adv. Energy Mater.* **14**, 2400943 (2024).
46. Bi, Z. et al. A surface-to-bulk tuning deep delithiation strategy for 5C fast-charging 4.6 V $LiCoO_2$. *Energy Environ. Sci.* **17**, 5706–5718 (2024).
47. Wang, J. et al. Toward direct regeneration of spent lithium-ion batteries: a next-generation recycling method. *Chem. Rev.* **124**, 2839–2887 (2024).
48. Abraham, M. J. et al. GROMACS: High performance molecular simulations through multi-level parallelism from laptops to supercomputers. *SoftwareX* **1–2**, 19–25 (2015).
49. Kaminski, G. A., Friesner, R. A., Tirado-Rives, J. & Jorgensen, W. L. Evaluation and reparametrization of the OPLS-AA force field for proteins via comparison with accurate quantum chemical calculations on peptides. *J. Phys. Chem. B* **105**, 6474–6487 (2001).
50. Bayly, C. I., Cieplak, P., Cornell, W. D. & Kollman, P. A. A well-behaved electrostatic potential based method using charge restraints for deriving atomic charges: the RESP model. *J. Phys. Chem.* **97**, 10269–10280 (1993).
51. Lu, T. & Chen, F. Multiwfn: a multifunctional wavefunction analyzer. *J. Comput. Chem.* **33**, 580–592 (2012).
52. Doherty, B., Zhong, X., Gathiaka, S., Li, B. & Acevedo, O. Revisiting OPLS force field parameters for ionic liquid simulations. *J. Chem. Theory Comput.* **13**, 6131–6145 (2017).
53. Martínez, L., Andrade, R., Birgin, E. G. & Martínez, J. M. PACKMOL: a package for building initial configurations for molecular dynamics simulations. *J. Comput. Chem.* **30**, 2157–2164 (2009).
54. Neese, F. Software update: the ORCA program system, version 4.0. *WIREs Comput Mol. Sci.* **8**, e1327 (2018).
55. Neese, F. Software update: the ORCA program system-version 5.0. *WIREs Comput Mol. Sci.* **12**, e1606 (2022).
56. Neese, F., Wennmohs, F., Becker, U. & Riplinger, C. The ORCA quantum chemistry program package. *J. Chem. Phys.* **152**, 224108 (2020).
57. Grimme, S., Antony, J., Ehrlich, S. & Krieg, H. A consistent and accurate ab initio parametrization of density functional dispersion correction (DFT-D) for the 94 elements H-Pu. *J. Chem. Phys.* **132**, 154104 (2010).
58. Momma, K. & Lzumi, F. VESTA 3 for three-dimensional visualization of crystal, volumetric and morphology data. *J. Appl. Cryst.* **44**, 1272–1276 (2011).

Acknowledgements

This work is financially supported by the National Natural Science Foundation of China (22179004 and 22261160570 to W.Z.), the National Key Research and Development Program of China (2022YFE0202400 and 2022YFA1204501 to W.Z.), the Natural Science National Natural Science Foundation of China, Basic Science Center Program (51988102 to L.Z.) and the Natural Science Foundation of Beijing (L223008 to W.Z.).

Author contributions

W.Z. designed this work. P.L., J.H., and Z.C. performed the experiments and analyzed the experimental results. S.H. performed the theoretical calculations. W.Z. and L.Z. wrote the manuscript. H.L., X.L., R.W., S.H., J.W., W.M., and Y.L. support the experiments and data analysis.

Competing interests

The authors declare no competing interests.

Additional information

Supplementary information The online version contains supplementary material available at https://doi.org/10.1038/s41467-025-59020-w.

Correspondence and requests for materials should be addressed to Weidong Zhou.

Peer review information *Nature Communications* thanks Jianhong Liu, Yuesheng Ning and the other, anonymous, reviewer(s) for their contribution to the peer review of this work. A peer review file is available.